

# Characterization of Multiphase Mixtures of Calcium Aluminates and Magnesium Aluminate Spinel Using Time-Gated Raman Spectroscopy

Francis Gyakwaa,\* Matti Aula, Tero Vuolio, Tuomas Alatarvas, Qifeng Shu, Marko Huttula, and Timo Fabritius

In aluminum-killed calcium-treated steels, the characterization of multiphase oxides found in the CaO–MgO–Al<sub>2</sub>O<sub>3</sub> system is essential for the study of inclusion formation, modification, and the control process. Herein, Raman spectroscopy is used as a characterization technique for the multiphase mixtures of MgO·Al<sub>2</sub>O<sub>3</sub> spinel and calcium aluminate phases of C12A7, C3A, and CA. Multiphase samples of C12A7–CA–MA and C12A7–C3A–MA are synthesized from MgO·Al<sub>2</sub>O<sub>3</sub> spinel and calcium aluminates with varying phase content. The relative intensity of the Raman peaks is qualitatively used for the most primary phases present in the sample. Regression models are also identified for predicting the phase composition. Prediction model identification is conducted using the successive projection algorithm (SPA) for feature selection and the partial least squares regression (PLS) model as a regressor. The identified prediction models show a reasonably good prediction performance. Herein, the time-gated Raman spectroscopy technique to characterize the multiphase mixture of magnesium aluminate spinel and calcium aluminate phases of CA, C12A7, C3A is used, and the potential application for inclusion characterization is demonstrated.

alumina, calcium aluminates, and MgO·Al<sub>2</sub>O<sub>3</sub> spinel. Inclusions with high alumina or spinel content possess some features such as low deformability, a high melting (liquidus) temperature, and an irregular shape.<sup>[3,4]</sup> In addition, the presence of these inclusions in steel may affect its quality and properties and increase the risk where submerged entry nozzles will become clogged during continuous casting.<sup>[2,5]</sup> To enhance the removal of inclusions, their flotation and absorption into the top slag have been extensively studied.<sup>[6–9]</sup>

Calcium treatment for Al-killed steels has been demonstrated to play a role in modifying Al<sub>2</sub>O<sub>3</sub> for calcium aluminate phases with a lower liquidus temperature compared with steel melt when controlled effectively.<sup>[10,11]</sup> Regarding steelmaking, the most relevant calcium aluminate phases are 12CaO·7Al<sub>2</sub>O<sub>3</sub> (C12A7), tricalcium aluminate, 3CaO·Al<sub>2</sub>O<sub>3</sub> (C3A), and monocalcium aluminate, CaO·Al<sub>2</sub>O<sub>3</sub> (CA).

The composition of C12A7 can be considered a target of calcium treatment, because it is fully liquid at steelmaking temperatures. The composition shift from C12A7 to C3A or CA increases the liquidus temperature and decreases the liquid fraction. In addition, studies have shown that calcium treatment can be used to modify MgO·Al<sub>2</sub>O<sub>3</sub> spinel inclusions.<sup>[12–14]</sup> However, the modification of Al<sub>2</sub>O<sub>3</sub> and spinel via calcium treatment may lead to the formation of inclusions in the MgO–Al<sub>2</sub>O<sub>3</sub>–CaO ternary system.<sup>[15–17]</sup> Deng and Zhu<sup>[15]</sup> and Yang et al.<sup>[16]</sup> also demonstrated that these inclusions might contain a MgO·Al<sub>2</sub>O<sub>3</sub> spinel phase enveloped with calcium aluminate phases. Calcium treatment may, therefore, result in the formation of multiphase inclusions containing calcium aluminates and MgO·Al<sub>2</sub>O<sub>3</sub> spinel.


The interest in inclusion studies in understanding the type, formation, and modification mechanisms has resulted in the use of various characterization techniques because this is of great importance for both the steel producer and product user. Scanning electron microscopy, coupled with energy-dispersive X-ray spectroscopy (SEM-EDS),<sup>[18,19]</sup> cathodoluminescence analysis,<sup>[20,21]</sup> and other characterization techniques outlined by other authors,<sup>[19,22]</sup> is commonly used. However, little has been discussed regarding the use of Raman for inclusion studies. Using a spectroscopic analytical technique such as Raman

## 1. Introduction

The evolution, modification process, and characterization of nonmetallic inclusions play a critical role in inclusion studies. In aluminum-killed calcium-treated steels, the common types of oxide inclusions identified by some researchers<sup>[1,2]</sup> include

F. Gyakwaa, Dr. M. Aula, T. Vuolio, Dr. T. Alatarvas, Prof. Q. Shu, Prof. T. Fabritius  
 Process Metallurgy Research Unit  
 University of Oulu  
 P.O. Box 4300, Oulu FI-90014, Finland  
 E-mail: Francis.gyakwaa@oulu.fi

Prof. M. Huttula  
 Nano and Molecular Systems Research Unit  
 University of Oulu  
 P.O. Box 4300, Oulu FI-90014, Finland

 The ORCID identification number(s) for the author(s) of this article can be found under <https://doi.org/10.1002/srin.202000084>.

© 2020 The Authors. Published by WILEY-VCH Verlag GmbH & Co. KGaA, Weinheim. This is an open access article under the terms of the Creative Commons Attribution License, which permits use, distribution and reproduction in any medium, provided the original work is properly cited.

DOI: 10.1002/srin.202000084

spectroscopy presents a promising characterization method for inclusion studies.<sup>[23,24]</sup> Raman spectroscopy has some relatively advantageous features compared with existing conventional inclusion characterization techniques, such as being a generally noninvasive, relatively fast, nondestructive analytical tool and making it possible to obtain the fingerprint of the specific component present in the sample (material).<sup>[25,26]</sup> In addition, Raman spectroscopy measurements have been demonstrated to be an instrument that may be used to conduct both qualitative and quantitative characterization for Raman-active materials.<sup>[27–30]</sup>

Calcium aluminate phases such as C12A7, C3A, and CA and magnesium aluminate spinel ( $\text{MgO}\cdot\text{Al}_2\text{O}_3$ ) have been shown to be Raman-active samples.<sup>[31–36]</sup> The author's previous research<sup>[37,38]</sup> also used Raman spectroscopy to characterize synthetic binary-phase samples containing calcium aluminate oxide phases and spinel. However, detailed characterization techniques for multiphase mixtures containing calcium aluminate and spinel phases using Raman spectroscopy are yet to be studied. Inclusion characterization from both laboratory and industrial steel samples analyzed with other characterization techniques shows that inclusions may occur as a mixture of phases or in multiphase.<sup>[16,17]</sup> In addition, the steel matrix is considered Raman inactive, demonstrating that if a Raman spectrum is acquired from a steel sample, it will originate from the inclusions found in steel. Using Raman spectroscopy as a characterization method for nonmetallic inclusions therefore requires further studies of the multiphase inclusion analyses relevant to steelmaking.

This study aims to demonstrate the application of time-gated Raman spectroscopy in the identification and quantitative characterization of synthetic multiphase samples that contain calcium aluminate phases of  $\text{CaO}\cdot\text{Al}_2\text{O}_3$  (CA),  $3\text{CaO}\cdot\text{Al}_2\text{O}_3$  (C3A),  $12\text{CaO}\cdot 7\text{Al}_2\text{O}_3$  (C12A7), and  $\text{MgO}\cdot\text{Al}_2\text{O}_3$  spinel (MA). Another aim is to examine the possible spectral effect of the multiphase samples prepared.

## 2. Experimental Section

Calcium oxide (CaO), aluminum oxide ( $\text{Al}_2\text{O}_3$ ), monocalcium aluminate  $\text{CaO}\cdot\text{Al}_2\text{O}_3$  (CA), and aluminate spinel  $\text{MgO}\cdot\text{Al}_2\text{O}_3$  (MA) were the chemicals used for this study. These chemical powders were obtained from Alfa Aesar, with purity in the range of 99.7–99.9%.

Calcium aluminate phase samples for C12A7 and C3A were prepared from CaO and  $\text{Al}_2\text{O}_3$  powders by weighing the appropriate CaO/ $\text{Al}_2\text{O}_3$  ratios, based on the CaO– $\text{Al}_2\text{O}_3$  binary system, and pressed into pellets. The pellets were sintered several times (sintering and regrinding) in a chamber furnace at 1350 °C to obtain the C12A7 and C3A phase samples.

To prepare the synthetic nonmetallic inclusion phase samples used for this study, the required proportions of calcium aluminate phase samples of  $\text{CaO}\cdot\text{Al}_2\text{O}_3$  (CA),  $3\text{CaO}\cdot\text{Al}_2\text{O}_3$  (C3A),  $12\text{CaO}\cdot 7\text{Al}_2\text{O}_3$  (C12A7), and spinel,  $\text{MgO}\cdot\text{Al}_2\text{O}_3$  (MA) were measured. These were followed by pressing the weighed samples into pellets and sintering them in a chamber furnace to achieve the phase fractions of interest. The sintering was conducted at 400 °C for moisture removal. The aim was to reduce the potential effect of moisture on the sample and ensure that it did not affect subsequent characterization.

The prepared pellets were milled into powder and analyzed using X-ray diffraction (XRD) and X-ray fluorescence (XRF). In addition, XRD analyses showed the suitability of the sintering temperature of 400 °C, because the phases remained unchanged after the moisture removal in the samples.

### 2.1. Sample Compositional Design

The synthetic inclusion phase sample mixtures were prepared according to a full factorial experimental design. This was conducted to reveal the individual effects and cross interactions of the Raman signal and the sample composition. A complete design matrix resulted in  $k^n$  compositions, where  $n$  is the number of components (design variables), and  $k$  is the number of design levels. Figure 1a,b shows that the overall number of samples was reduced by selecting the compositional areas of interest, based on the potential liquidus regions. The total number of samples was 43 for MA–C12A7–C3A and 48 for C12A7–CA–MA. The samples were further grouped as A, B, and C, the characteristics of which are explained as follows: 1) *Group A* sample mixture contained various phase fractions for the calcium aluminate phases of C3A and C12A7 with fixed phase fraction for the spinel, as shown in Figure 1(i). In Figure 1a,b(i) also had the phase content for CA, and C12A7 was varied and maintained the same phase fraction for MA. 2) *Group B* contained the sample mixtures, in which the individual phase fraction was varied, based on the sample matrix of interest (MA–C12A7–C3A and C12A7–CA–MA). Figure 1a(ii),b(ii) shows the sample matrix. 3) *Group C* fixed the phase fraction for the calcium aluminate phases used in this study at a given weight percentage and a changing weight percentage for MA. Figure 1a(iii) shows the sample mixture for MA–C12A7–C3A. Figure 1b(iii) shows it for a sample mixture matrix consisting of C12A7–CA–MA. The sample matrix was designed to examine the possibility of applying Raman spectroscopy to characterize these synthetic inclusion phases under varying phase fraction conditions, as shown in Figure 1a(iv),b(iv).

### 2.2. Analytical Techniques

#### 2.2.1. X-Ray Fluorescence and X-Ray Diffraction

XRF elemental analysis was conducted on the prepared samples to verify the chemical composition. XRF provides the weight percentage of the identified elements. The XRF instrument used for this study was the Panalytical Axios Max model, with a set-up consisting of an X-ray generator Rh tube and a maximum power of 4 kW. The analysis software used for elemental analysis was SuperQ.

A Rigaku SmartLab 9 kW XRD instrument was used for sample phase identification. XRD measures the intensity of the crystal diffraction peaks as a result of the individual chemical compounds and the phase identification in the sample. The instrument is made of Bragg–Brentano parafocusing geometry (300 mm goniometer) and a Cu source lamp with 45 kV and 200 mA settings (9 kW rotating anode) and an acquisition speed of 3° per minute with 0.02° per step. Additional features include a 10 mm limiting slit located at the source side of the samples in

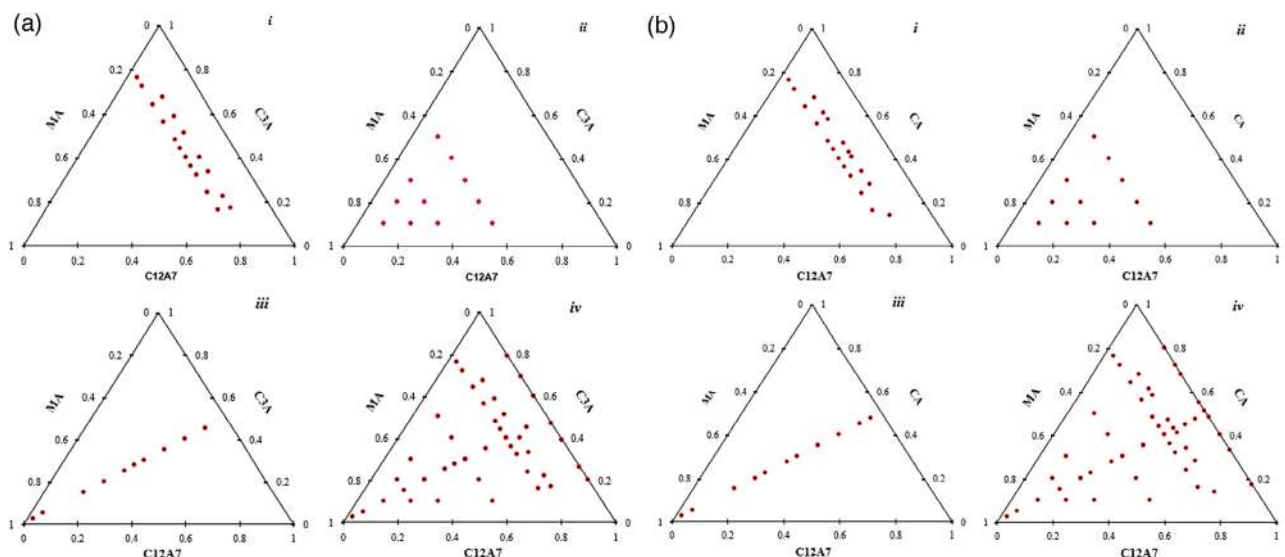


**Figure 1.** a) Sample matrix for C3A–C12A7–MA used in this study where there is: i) a varying phase fraction for C3A–C12A7 with a fixed content of MA; ii) a varying phase content for C12A7, MA, and C3A; iii) a fixed content for C3A and C12A7 with a varying content for MA; and iv) a total number of the sample for C3A–C12A7–MA. b) Sample matrix for CA–C12A7–MA used in this study where there is: i) a varying phase fraction for CA–C12A7 with a fixed content of MA; ii) a varying phase content for C12A7, MA, and CA; iii) a fixed content for CA and C12A7 with a varying content for MA; and iv) a total number of the sample for C3A–C12A7–MA.

standard glass holders and 5° Soller slits used on both sources and the analyzer side. XRD analysis to evaluate the weight percentage for the phases present in the samples was conducted using PDXL2 software suite with integrated access to PDF-4 2018 database.

Using XRD and XRF as sample characterization methods may be complementary techniques in verifying the initial prepared sample's composition.

### 2.2.2. Raman Spectroscopy

Raman spectroscopy is an example of a vibrational spectroscopic technique that operates based on the introduction of laser radiation to create an inelastic scattering of monochromatic light to the Raman active sample.<sup>[25,26]</sup> The Raman spectra provide information in which the peak represents the change in energy of the scattered laser interaction with the material measured. The measured Raman spectrum serves as a fingerprint for the individual component present in the sample. In addition, the reason for considering Raman spectroscopy for quantitative estimation may be based on the proportional relationship between the analyte concentration in the sample and the Raman scattering intensity.<sup>[25,26,29,30]</sup>

As an analytical technique for characterization, Raman spectroscopy continues to find its application in most iron and steel-making research fields, such as slag structural characterization and viscosities studies.<sup>[39]</sup> Raman spectroscopy is also applicable as a characterization technique in other research areas: an example is the pharmaceutical sector.<sup>[29,30]</sup>

A TimeGated 532 Raman spectrometer (TG532 Model1) provided by TimeGated Instruments Ltd., Finland, was used to acquire the Raman spectra from the sample mixtures. The

Raman instrument set-up is equipped with a complementary-metal-oxide-semiconductor (CMOS) single-photon avalanche diode (SPAD) array detector, a picosecond pulsed laser, and a BWTek sampling probe. The excitation source was a pulsed laser of 532 nm, with Photonics RPB532 w/105 μm excitation fiber. The probe head was made of 200 μm collection fiber, with a spot size of 1 mm. Other components included fiber coupling, with a shot length of 150 ps and a frequency range from 40 to 100 kHz, a fiber-coupled spectrograph, and delay electronics.

TimeGated Raman technology provides additional features such as real fluorescence rejection and the ability to prevent other photoluminescence phenomena compared with the Achilles' heel of conventional Raman technology.<sup>[40]</sup> This technology from TimeGated Raman helps reduce the potential interference of these phenomena with the Raman signal measured from the sample.

A spectra acquisition time of 3–5 min and Raman spectra range of 100–1200 cm<sup>-1</sup> with a resolution of 10 cm<sup>-1</sup> were used in this work for the sample measurements. A good reproducibility for the acquired Raman spectra was conducted by measuring the samples several times. A rotating sample holder stage was used to obtain spatially averaged spectra from the measurement. Data acquisition and preprocessing were carried out with the instrument software (TimeGated Model 1) provided by the TimeGated Raman company.

### 2.3. Prediction Model Selection

The model selection problem is divided into four sequential steps: data treatment, feature selection, model training, and model performance evaluation. Prior to feature selection and data normalization, the data were split into training and external

validation sets, of which the training set alone was used for model identification. The division was conducted such that 10% of the data were selected randomly for external validation. After the initial treatment of the signal, described in Section 2.1.2, each of the spectra was standardized such that  $\mu_X = 0$  and  $\sigma_X = 1$  to increase comparability. The need for the normalization of Raman spectral datasets was highlighted in the study of Beattie et al.<sup>[41]</sup> To evaluate the repeatability for the model selection, the whole procedure was repeated  $2N$  times.

To yield more interpretable and stable calibration models, a feature selection was conducted to reduce the data's dimensionality. In prediction model identification, feature selection is usually conducted to improve the prediction performance and speed, as well as to increase the interpretability.<sup>[42]</sup> In the context of spectral analysis, the usual objective of feature selection is to extract the signal's relevant information to estimate the phase composition in the samples.<sup>[43]</sup> It is discussed in the literature that the performance of the PLS models can be improved with the feature selection.<sup>[44]</sup> In the model and feature selection, the objective of the feature selection is to use minimum information on the signal with which the maximal prediction performance is achieved. The problem of feature selection can be solved by applying deterministic search engines using a suitable objective function. In this study, the objective function is based on the prediction error for the internal validation set. It should be noted that the internal validation set is often referred to in the literature as the cross-validated set.<sup>[44]</sup> In other words, the objective is to

$$\min J(\mathbf{b}, X) = \min \sum_{i=1}^k (y_{i,iv} - f(\mathbf{b}, X_{i,iv}))^2 \quad (1)$$

where  $J$  is the objective function,  $\mathbf{b}$  is the model parameter vector,  $X$  is a matrix with  $k$  columns and  $n$  rows, and  $f$  is the functional relationship with the signal features. The objective function is minimized with a suitable solution strategy. In this study, the successive projection algorithm (SPA) was used as the search engine. SPA was categorized as a deterministic forward selection method. A property of deterministic search engines is that a combination that gives a smaller error than all the previous tested combinations is treated as the best combination of features.

In the SPA, the feature set candidates were models that were initialized for each of the single feature models. The index of a next feature to be added in the projection phase was chosen such that the feature  $j = \operatorname{argmax} \|Px_j\|$ , where  $P$  is the projection operator computed with the Gram-Schmidt orthogonalization process. This provided that each of the feature candidate sets was chosen such that the loading of the covariance matrix was maximal. After a feature was added, the next projection was computed. This was repeated until the predetermined number of features was reached.

Consequently, after a projection phase, we had a pool of models corresponding to the number of features available in the dataset. After the projection phase, each of the model candidates was validated with the hold-out cross-validation. The amount of data in each of the internal validation repetitions was 30% of the training data. The model that gave the smallest cross-validation error and the smallest number of variables/features for the objective function was chosen as the final model.

It was shown that the SPA usually selected the relevant features and tended to minimize the collinearity within the selected feature set. The algorithm had proven effective in feature selection tasks from spectroscopic data.<sup>[45]</sup>

After feature selection, a partial least squares regression (PLS) model was trained to the data. PLS regression was used intensively for spectral calibration. An exhaustive description of PLS regression was found in the study by Geladi and Kowalski,<sup>[46]</sup> so it is not repeated here. The number of latent variables for the PLS model was selected such that the mean absolute error (MAE) for the internal validation set was minimized. It should be noted that the maximum number of latent variables now corresponded to the number of wavelengths selected by the SPA. The final performance of the model was assessed with the external validation dataset using standard figures of merit, being a coefficient of determination ( $R^2$ ) and MAE.

### 3. Results and Discussion

#### 3.1. XRD and XRF Characterization

Figure 2 shows the XRD spectra measured from the starting synthetic phase samples used in this study, where *i*, *ii*, *iii*, and *iv* correspond to CA, C3A, MA, and C12A, respectively. Table 1 shows the comparison between XRD-calculated elemental compositions and XRF-measured values, estimated based on their weight percentages (wt%) for CaO and Al<sub>2</sub>O<sub>3</sub>.

The CaO and Al<sub>2</sub>O<sub>3</sub> weight percent for C12A7 and C3A were estimated based on the molar mass of 12CaO·7Al<sub>2</sub>O<sub>3</sub> for C12A7, 3CaO·Al<sub>2</sub>O<sub>3</sub> for C3A, and the phase percentage (wt%) obtained from the XRD analysis. Some assumptions were made in comparing these two (XRF and XRD) analysis results. Samples analyzed by XRD were considered to have stoichiometric phases. The XRD data were normalized in evaluating phase fraction to elemental compositions and then compared with the XRF

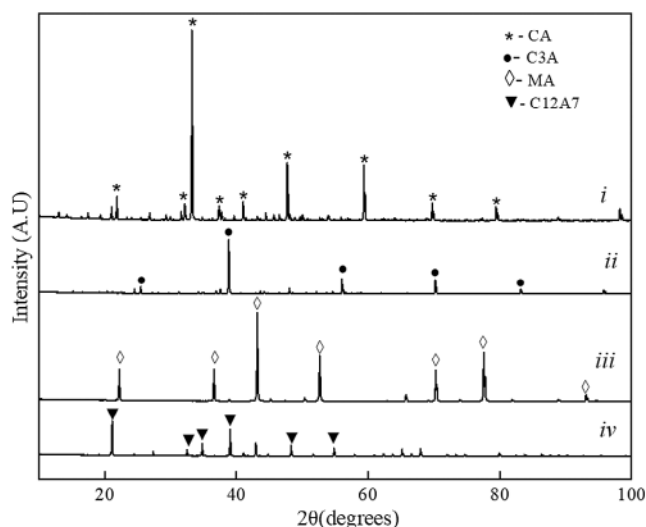


**Figure 2.** XRD spectra for the starting sample phases, where *i*) is for the CA phase, *ii*) is for the C3A phase, *iii*) is for the MA phase, and *iv*) corresponds to the C12A7 phase.

**Table 1.** XRD and XRF analyses for sample mixture of calcium aluminate phases of C12A7, C3A, and MgO·Al<sub>2</sub>O<sub>3</sub> (MA) spinel.

XRD analysis [wt%]			Calculated from XRD results [wt%]		XRF analysis [wt%]			Difference between XRD and XRF [wt%]
C12A7	C3A	MA	CaO	Al <sub>2</sub> O <sub>3</sub>	CaO	Al <sub>2</sub> O <sub>3</sub>	MgO	CaO
48	11	41	30.49	29.51	33.38	56.60	10.03	-1.86
32	26	42	33.24	26.76	35.52	53.87	10.61	-2.28
12	45	43	35.98	22.64	38.43	51.40	10.17	-2.44
32	10	58	20.79	15.09	25.38	60.55	14.07	-3.63
19	16	63	22.16	17.84	25.52	60.05	14.43	-3.36
11	26	63	23.53	16.47	25.88	59.50	14.63	-2.34

results. All CaO present in the samples analyzed with XRF were assumed to be associated with the calcium aluminate phases identified with the XRD. In addition, it was assumed that for the XRF results, all the Mg (MgO) present in the sample elemental composition analysis could be attributable to the presence of the MgO·Al<sub>2</sub>O<sub>3</sub> (MA) spinel phase fraction in the sample. These assumptions enable a more straightforward comparison between XRD and XRF. Both instruments used for sample characterization serve as a complementary technique that provides phase fraction (XRD) and elemental information (XRF) to verify the sample composition.

### 3.2. Raman Spectra Analysis

Table 2 shows the identifiable Raman shift or bands (cm<sup>-1</sup>) for the prepared synthetic inclusion phases (CA, C12A7, C3A, and spinel MgO·Al<sub>2</sub>O<sub>3</sub>). The Raman shifts identified for the individual phases in this work correspond with previous studies.<sup>[31–36]</sup> The Raman shift between what was measured in this work and the reference literature falls within a range of ±5 cm<sup>-1</sup>. Figure 3 shows the Raman spectra for synthetic phases of CA, C12A7, C3A, and spinel MgO·Al<sub>2</sub>O<sub>3</sub> used to prepare multiphase mixtures of C3A–C12A7–MA and C3A–C12A7–MA. The Raman peaks observed at 525 cm<sup>-1</sup> for CA, 508 cm<sup>-1</sup> for C3A, and 522 cm<sup>-1</sup> for C12A7 are assigned to symmetric stretching of the Al–O bonds found in AlO<sub>4</sub><sup>5-</sup> groups or bridged oxygens in the Al–O–Al linkages.<sup>[37,47]</sup> The Raman peaks located at 772 cm<sup>-1</sup> for C12A7, 790 cm<sup>-1</sup> for CA, and 756 cm<sup>-1</sup> for C3A are attributed to asymmetric stretching modes observed in AlO<sub>4</sub><sup>5-</sup> tetrahedra.<sup>[37,47]</sup> These characteristic vibration modes of the bonded framework Al–O distinguish the difference in phases in the calcium aluminate system. MgO·Al<sub>2</sub>O<sub>3</sub> spinel that have Raman bands observed at 416 cm<sup>-1</sup> is assigned to the bending mode of Al ions found in tetrahedral sites, and 674 cm<sup>-1</sup> is

**Table 2.** Reference and measured Raman shift (cm<sup>-1</sup>) for calcium aluminate and spinel phases (where s is strong, m is medium, and w is weak).

Phase	Measured peaks [Raman shift, cm <sup>-1</sup> ]	Reference [Raman shift, cm <sup>-1</sup> ]	Reference
CA	525 s, 549 m, 790 w	520–521 s, 545–547 m, 790–793 w	[34–36]
C12A7	522 s, 781 m, 314 m	312–333 m, 516–517 m, 772 m, 779 m	[34–36]
C3A	756 s, 508 m	756–757 s, 140–150 w, 506–508 m	[3–36]
MgO·Al <sub>2</sub> O <sub>3</sub>	416 s, 674 m, 773 m	409–412 s, 767–772 m, 666–674 m, 312–313 m	[31,32]

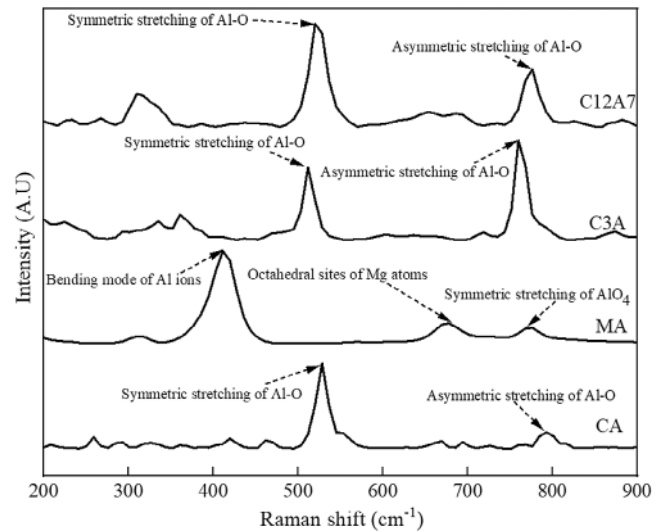


**Figure 3.** Raman spectra for the starting sample phases of C12A7, C3A, MA, and CA used to prepare ternary samples of C3A–C12A7–MA and C12A7–MA.<sup>[31,32,37,47]</sup>

attributed to bands that can be attributed to bending motion in octahedral sites of Mg atoms.<sup>[31,32]</sup> In addition, Raman peak was observed at 773 cm<sup>-1</sup>, the symmetric associated with stretching of AlO<sub>4</sub> in tetrahedral sites.<sup>[31,32]</sup>

### 3.3. Qualitative Analysis of the Raman Spectra

Figure 4–6 shows some examples of Raman spectra measured from the multiphase samples, where the phase content (wt%) had a corresponding effect on the Raman peak intensities. Qualitatively, the peaks' relative intensity could be used to estimate phases with a higher content in the sample. Using variation in phase content (wt%) in the samples measured with the Raman spectroscopy and observing the change in the peaks' relative Raman intensity for the phases present in the sample, therefore, offer the opportunity to examine a sample qualitatively.

#### 3.3.1. Raman Spectra for Fixed Content of MgO·Al<sub>2</sub>O<sub>3</sub> and Varying CaO·Al<sub>2</sub>O<sub>3</sub> Phases

Raman spectra obtained from a set of sample matrix mixtures that contain approximately fixed weight percentages (wt%) for MgO·Al<sub>2</sub>O<sub>3</sub> (MA) are added to binary calcium aluminate phase samples of C12A7–C3A and C12A7–CA. The aim is to examine any potential observations that could be noticed in comparing

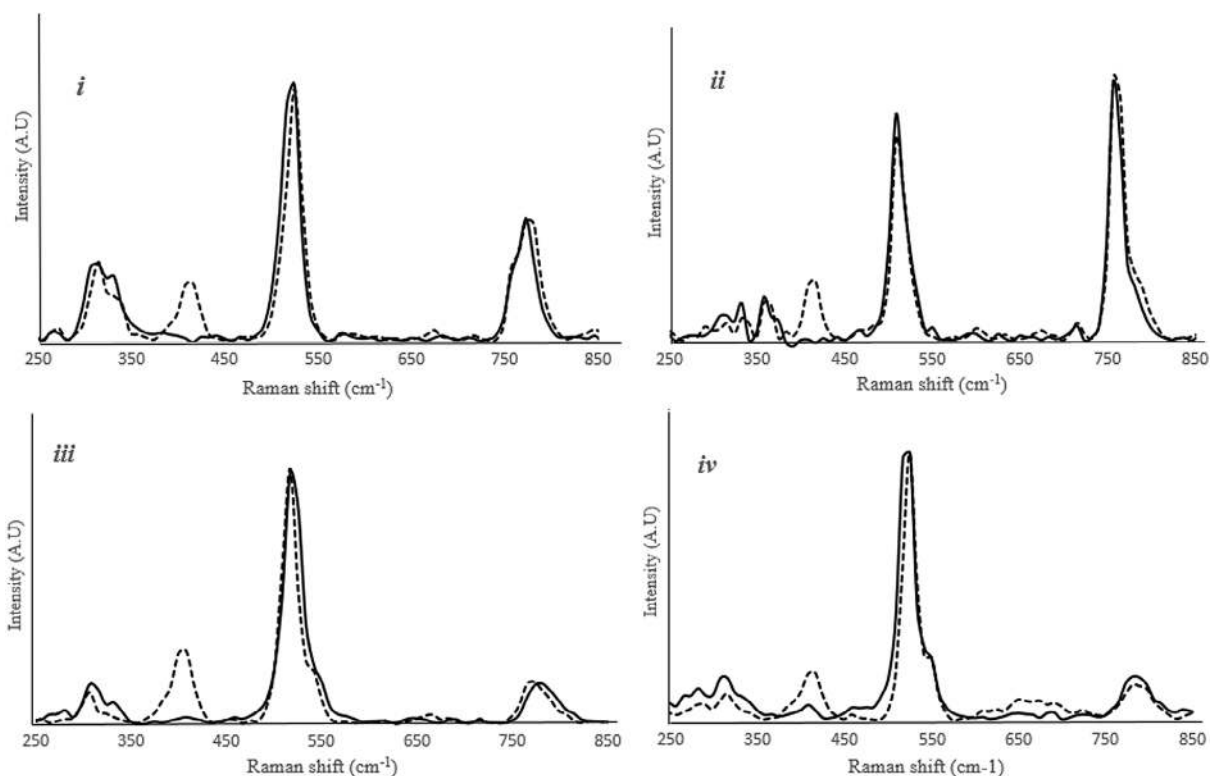


**Figure 4.** Raman spectra for binary and ternary (spectra marked with dotted line) samples, where *i*) and *ii*) are for C12A7-C3A and C3A-C12A7-MA; *iii*) and *iv*) represent C12A7-CA and CA-C12A7-MA samples.

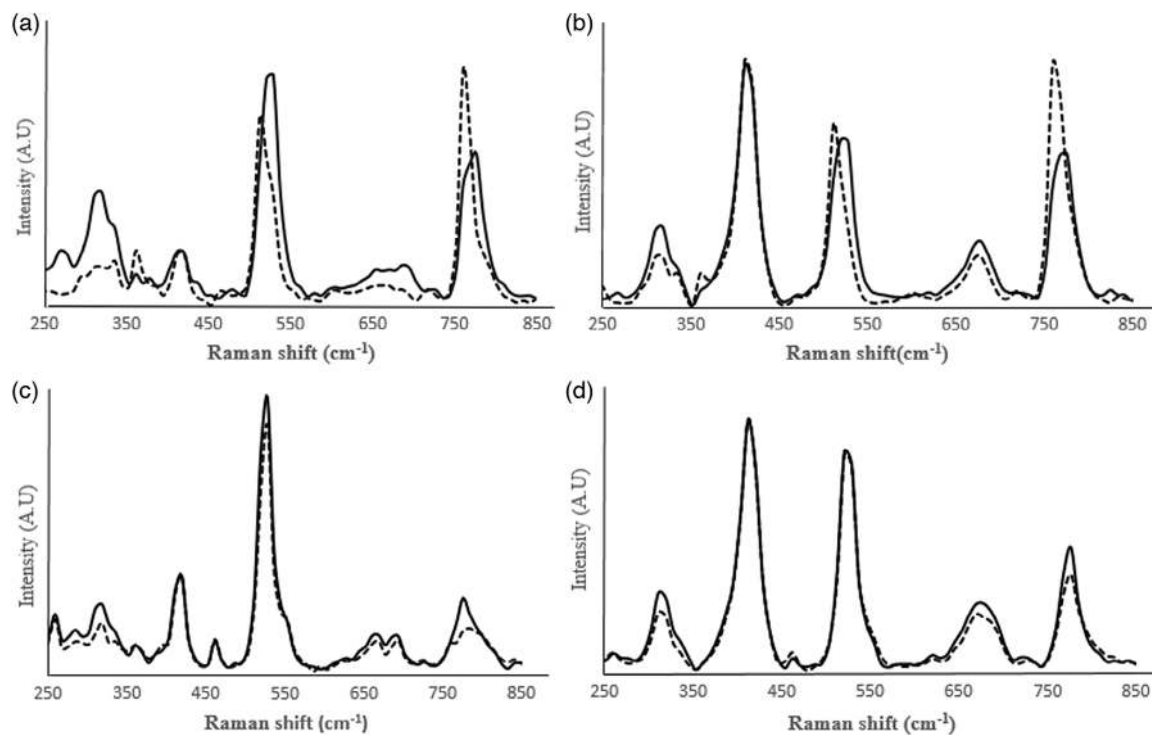


**Figure 5.** Raman spectra for multiphase samples showing different sample matrices, where a,b) are for C3A-C12A7-MA, and c,d) represent CA-C12A7-MA samples.

the Raman spectra for the binary and ternary samples formed with the introduction of the spinel phase.

Figure 4 shows the Raman spectra for a set of binary phase samples indicated by a solid line and ternary samples indicated by a dotted line. Figure 4(i,ii) shows a set of Raman spectra for a binary phase of C12A7–C3A and ternary phase of C3A–C12A7–MA, and Figure 4(iii,iv) shows a pair of Raman spectra for both binary samples of C12A7–CA and the multiphase of CA–C12A7–MA. About 20 wt% of MgO·Al<sub>2</sub>O<sub>3</sub> (MA) was added to the binary phase of C12A7–C3A and C12A7–CA to produce C3A–C12A7–MA and CA–C12A7–MA, as shown in Table 3, where the italic and bold values represent the multiphase compositions.

Figure 4 shows an introduction of the MgO·Al<sub>2</sub>O<sub>3</sub> (MA) phase to binary phase samples of C12A7–C3A, and the C12A7–CA sample shows a Raman shift peak in the region of 410–420 cm<sup>-1</sup>, indicating the presence of MA. This peak is associated with the MgO·Al<sub>2</sub>O<sub>3</sub> spinel phase found in the ternary sample for C3A–C12A7–MA and CA–C12A7–MA, because the same Raman peak could not be seen for samples containing only C12A7–C3A and C12A7–CA. Similar observations could also be made for binary sample peaks, which had almost the same relative intensity as peaks found in the spectra of the ternary samples.

In addition, it is noticeable from both binary (C12A7–C3A) and ternary (C3A–C12A7–MA) samples Raman spectra in Figure 4(i,ii) that an increase in Raman shift in the region of 517–522 cm<sup>-1</sup> had a corresponding increment in the phase fraction for C12A7. This increase is a feature of C12A7 because the most intense peak for this phase is located around 517–522 cm<sup>-1</sup>. It is also observable from the spectra in Figure 4(iii,iv) that an increment in the C12A7 phase fraction for C12A7–CA and CA–C12A7–MA samples exhibits a corresponding increase in the Raman shift in the region of 776–781 cm<sup>-1</sup>, a medium Raman peak for C12A7.<sup>[34–36]</sup> Similarly, an increase in C3A content in both sets (C12A7–C3A and C3A–C12A7–MA) of the Raman spectra shows a corresponding increase in the Raman peak intensity in the region of 756–765 cm<sup>-1</sup>, which is associated with C3A.

Furthermore, for C12A7–CA and CA–C12A7–MA samples, an increased CA content shows an increase in the peak shoulder intensity in the region of 545–549 cm<sup>-1</sup> for the spectra shown in Figure 4(iii,iv). The most intense Raman peak for CA and C12A7 could not be used directly for C12A7–CA and CA–C12A7–MA, and the changes in the phase content due to potential peak overlapping for the most intense peaks were distinguished because it was not readily observable. Qualitatively, the appearance of

medium peaks in the region of 776–781 cm<sup>-1</sup> for C12A7 and 545–549 cm<sup>-1</sup> for CA for the sample's analysis could therefore be considered most suitable.

### 3.3.2. Observations from Raman Spectra Multiphase Mixture with Varying Phase Content

This subsection examines the Raman spectra for the ternary system for C3A–C12A7–MA and CA–C12A7–MA in which all the phase content is varied. This is to qualitatively determine how the changes in phase content may be related to the Raman spectra obtained from the samples.

Figure 5a,b shows Raman spectra for C3A–C12A7–MA with varying phase fractions for C12A7, C3A, and MA, and in Figure 5c,d, the multiphase sample of CA–C12A7–MA, with varying phase content for C12A7, CA, and MA, is shown. Table 4 shows the sample matrix data for the Raman spectra shown in Figure 5. The italic and bold values are used to represent the Raman spectra for the ternary compositions with dotted lines in Figure 5.

The weight percentage for MA in the ternary sample for C3A–C12A7–MA and CA–C12A7–MA was ≈60 wt% for Figure 5a,c and 20% for Figure 5b,d. It is observed that there is a relative intensity for the peak changes with a corresponding variation in content for a specific phase present. The Raman spectra also demonstrate that when phase fraction for MA in the sample varies, a similar trend is observed in a change in the relative intensity of the peak within the Raman shift in the region of 410–420 cm<sup>-1</sup>.

Calcium aluminate phases for C12A7, CA, and C3A showed a similar change in relative peak intensity based on specific phase content variation. C3A had the most intense peak within the Raman shift in the region of 756–765 cm<sup>-1</sup>, and Figure 5b shows that it increased when the phase fraction for C3A in the sample increased. In addition, this phenomenon could also be observed for C12A7 in the multiphase sample, where an increase in this phase content in the sample demonstrated a noticeable increase in the peak intensity Raman shift in the region of 517–522 cm<sup>-1</sup>. There is the potential for a slight overlap to occur between C12A7 and C3A, because the most intense peak for C12A7 was within the region of 517–522 cm<sup>-1</sup>, and the medium peak for C3A found at Raman shift (band) was in the region of 508–512 cm<sup>-1</sup>. The most intense Raman peak for C3A at 756–765 cm<sup>-1</sup> and the medium peak for C12A7 found around the Raman shift in the region of 776–781 cm<sup>-1</sup> also had the potential to overlap.

For CA–C12A7–MA samples, it was observed that with an increasing phase content for C12A7 in the ternary mixture, the medium peak within the Raman shift in the region of 776–781 cm<sup>-1</sup>, showed an increase in relative intensity. A similar trend could be observed for CA, where an increase in the phase fraction showed a corresponding increase in the appearance of the shoulder peak at ≈549 cm<sup>-1</sup>.

### 3.3.3. Raman Spectra for C12A7 Fixed Phase Content

The work considered in this subsection observes the Raman spectra pattern that could be obtained by approximately fixing a specific phase content of calcium aluminate while varying

**Table 3.** Sample matrix data for binary (C12A7–C3A and CA–C12A7) and ternary (C3A–C12A7–MA and CA–C12A7–MA) samples values for the Raman spectra shown in Figure 4. The italic and bold values show the ternary compositions.

Label	C12A7	C3A	MA	Label	C12A7	CA	MA
<i>i</i>	30	70	0	<i>iii</i>	83	17	0
	<b>20</b>	<b>20</b>	<b>60</b>		<b>71</b>	<b>14</b>	<b>15</b>
<i>ii</i>	64	36	0	<i>iv</i>	20	80	0
	<b>24</b>	<b>56</b>	<b>20</b>		<b>17</b>	<b>68</b>	<b>15</b>

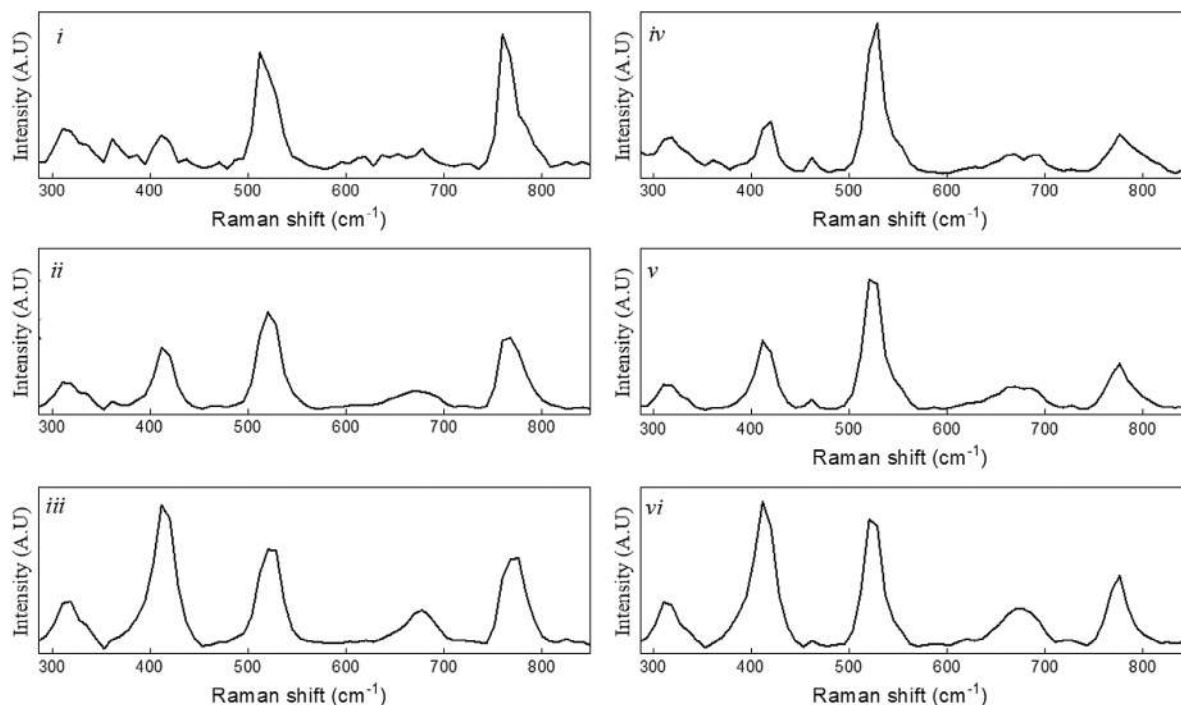


**Figure 6.** Raman spectra for multiphase C3A–C12A7–MA and CA–C12A7–MA, where *i*) 60MA–30C12A7–10C3A, *ii*) 40MA–30C12A7–30C3A, *iii*) 20MA–30C12A7–50C3A, *iv*) 60MA–30C12A7–10CA, *v*) 40MA–30C12A7–30CA, and *vi*) 20MA–30C12A7–50CA.

**Table 4.** Sample matrix data for binary multiphase mixture samples (C3A–C12A7–MA and CA–C12A7–MA) for the Raman spectra shown in Figure 5. The italic and bold values represent the Raman spectra for the multiphase compositions with dotted lines in Figure 5.

Label	C12A7	C3A	MA	Label	C12A7	CA	MA
<u><i>a</i></u>	<b>10</b>	<b>30</b>	<b>60</b>	<u><i>c</i></u>	30	10	60
	30	30	60		<b>10</b>	<b>30</b>	<b>60</b>
<u><i>b</i></u>	64	16	20	<u><i>d</i></u>	64	16	20
	<b>10</b>	<b>70</b>	<b>20</b>		<b>10</b>	<b>70</b>	<b>20</b>

the other phase content in a multiphase sample system. C12A7 is used to illustrate this phenomenon by selecting approximately a fixed phase content and varying MA, C3A, and CA components. This phase (C12A7) was selected because it was the most desirable inclusion compared with the others because of its lower melting temperature.

Figure 6 shows some examples of Raman spectra for the C12A7 phase component at  $\approx 30$  wt%, with a varying phase ratio for CA, C3A, and MA. Figure 6(*i–iii*) is for samples containing C3A–C12A7–MA, and Figure 6(*iv–vi*) shows a ternary sample of CA–C12A7–MA. An increment or change in the phase content for MA reflects an increase in relative intensity at around  $416\text{ cm}^{-1}$ , as explained in the previous figures.

Furthermore, C12A7 maintained at  $\approx 30$  wt% for sample mixtures of C12A7–CA–MA and C12A7–C3A–MA demonstrates that a relative intensity variation for this corresponds to how the specific phase content in the sample changes. Figure 6

confirms the observations shown in Figure 4 and 5 regarding how the Raman peak intensity varies with the sample’s changing phase fraction. These illustrations therefore demonstrate that Raman spectroscopy can be used for a qualitative analysis based on the change in content for a specific phase that has a corresponding change in the relative intensity for the peak assigned to each phase present in the sample.

### 3.4. Quantitative Estimation of the Phase Fractions in the Samples

In Table 5, the quantitative figures of merit, namely, the coefficient of determination ( $R^2$ ), and MAE for each of the phases existing in the samples, are presented. It should be noted that the figures of merit are presented separately for each of the datasets. Based on the results of the model identification, it is obvious that

**Table 5.** Figures of merit for each of the calibration models measured with different data splits.

Phase <sup>a)</sup>	$R_t^2$	MAE <sub>t</sub>	$R_{iv}^2$	MAE <sub>iv</sub>	$R_{ev}^2$	MAE <sub>ev</sub>	$n_f$	$n_{lf}$
C12A7	0.93	2.76	0.96	3.77	0.96	3.44	5	5
C3A	0.96	2.63	0.96	3.54	0.97	3.07	6	4
MA	0.97	3.13	0.99	2.31	0.97	2.31	15	10
CA	0.96	2.62	0.96	2.72	0.96	3.75	10	9

<sup>a)</sup>Note: t = training set, iv = internal validation set, ev = external validation set, f = features, lf = latent features.



the variance in the samples can be explained using only 5–15 signal wavelengths, which results as parsimonious and interpretable models compared with the case in which the full spectrum is used for model parameter identification. Consequently, the dimensions of the data have reduced 5–17% of the original dataset with feature selection. Table 5 shows that it can be observed that MAE varies between 2.31 and 3.75 wt% for external validation sets, depending on the phase of interest, which is very encouraging where the applicability of time-gated Raman spectroscopy in the control of steel cleanliness is concerned.

In **Figure 7**, the measured and predicted values are presented for each of the systems. It shows that the predictions for each of the phases of this study are consistent, and the data points are spread evenly around the diagonal. This indicates that the selected model may explain the variance in the training data and generalize well to the external validation set. However, the prediction performance depends greatly on the normalization method: to exemplify, the corresponding figures of merit for C12A7 phase are  $R_2 = 0.6$  and MAE = 9.6 wt% for the external dataset. The effect of normalization on the prediction results resembles the results reported in the study by Beattie et al.<sup>[41]</sup>

and our previous studies, in which the relative intensity was used to normalize the peak intensities.

**Figure 8** shows the feature selection results for 2N repetitions of the SPA. Each of the repetitions was conducted using a different split for training and internal validation data. The selection frequencies for each of the Raman shifts are presented as bars and compared with a randomly selected non-normalized signal. Basically, if the feature repeatedly occurs in the selection, it can be considered interesting in some way. In this study, all the shifts that occurred for more than 30% of cases were considered of interest. Consequently, the areas of interest for each of the phases are as follows: C12A7: 318–335, 419–428, 520–536, and 768–784  $\text{cm}^{-1}$ ; C3A: 419–428, 536, and 768–784  $\text{cm}^{-1}$ ; MA: 259, 293, 419–428, 536, 768–784  $\text{cm}^{-1}$ ; and CA: 259, 326, 419–428, 536, 768–784  $\text{cm}^{-1}$ .

It can be seen from the selection results that there is a slight overlapping in the selected shifts. In addition, a multivariable model performs better than a simple regression between the signal and the reference data. In other words, more features/variables explain the variance in the phase concentration better than a single peak model does. This is because the covariance

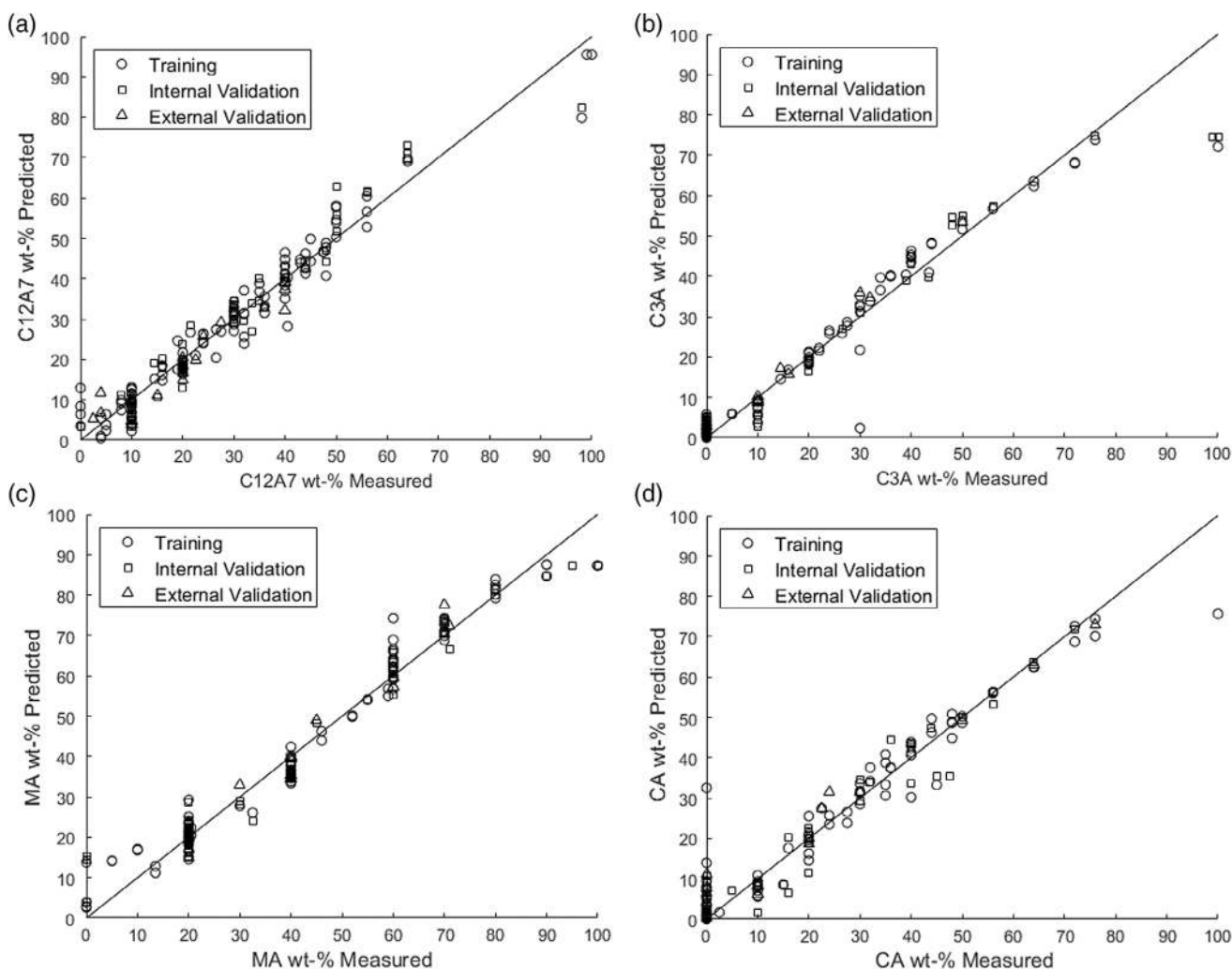


**Figure 7.** Predictions for the phase fractions. a) C12A7 wt%, b) C3A wt%, c) MA wt%, and d) CA wt%.

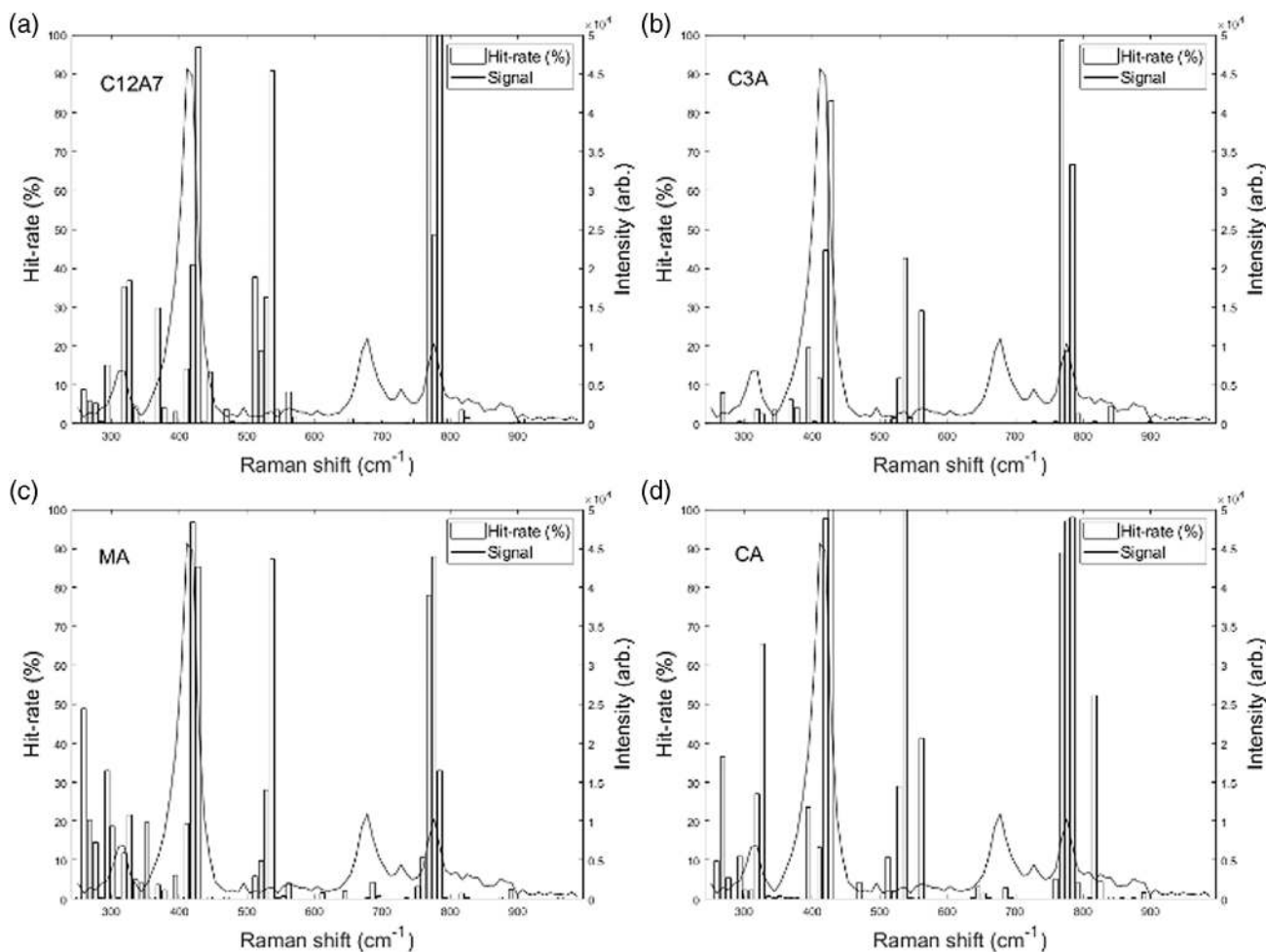


**Figure 8.** Selected features for 2N repetitions compared with a randomly selected signal for illustration. a) C12A7 wt%, b) C3A wt%, c) MA wt%, and d) CA wt%.

between individual peaks and the phase concentrations is not strong and stable enough, and to capture the variance, one must use more features of the signal. The overlapping itself does not indicate that the same peaks are related to the existence of a certain component in the sample but only that the selected peaks help in explaining the variance in the phase fraction. This is because the following holds for the binary and ternary systems:  $\alpha + \beta = 1$  and  $\alpha + \beta + \gamma = 1$ . However, as shown in Figure 3, the Raman shifts for different calcium aluminates have some overlaps in peaks.

### 3.5. The Potential Source of Error in the Measurements

Using vibrational spectroscopic techniques such as Raman spectroscopy may have some disadvantages. For example, there may be a slight instrumental disadvantage, causing operational challenges such as a variation in incident laser power and a response to the detection system during sample measurements. This may cause a slight shift in the position of the Raman peaks or overlapping peaks for the phases present in a sample. In addition, fluorescence-sensitive samples may also affect the quality of

the measured Raman spectra. However, no effect of potential fluorescence on the measured samples was encountered and using time-gated Raman spectroscopy reduced this effect.

### 3.6. Prospect for Practical Application

Studies conducted on a MgO–Al<sub>2</sub>O<sub>3</sub>–CaO system for both laboratory and industrial steel samples suggest that, depending on the modification and control process, different multiphase inclusions may be formed. Researchers<sup>[15,17,48–52]</sup> demonstrated a general pattern for inclusion evolution for Al-killed calcium-treated steels and a potential source of Mg from refractory or slag. A simple schematic evolution process is shown in **Figure 9** and describes Al<sub>2</sub>O<sub>3</sub>→MgO·Al<sub>2</sub>O<sub>3</sub> (MA)→ CaO·Al<sub>2</sub>O<sub>3</sub> (CA)→ MgO·Al<sub>2</sub>O<sub>3</sub>–(CaO)<sub>x</sub>(Al<sub>2</sub>O<sub>3</sub>)<sub>y</sub>, studied by others.<sup>[15,17,48–52]</sup> Figure 9 shows a the potential route which illustrates the modification process for generating a multiphase system consisting of a solid MgO·Al<sub>2</sub>O<sub>3</sub>, (CaO)<sub>x</sub>(Al<sub>2</sub>O<sub>3</sub>)<sub>y</sub>, and (CaO)<sub>x</sub>(Al<sub>2</sub>O<sub>3</sub>)<sub>y</sub>(MgO)<sub>z</sub> for Al-killed calcium-treated steel. Figure 9(i) shows the deoxidation process done by introducing Al into the molten steel and the potential formation of solid Al<sub>2</sub>O<sub>3</sub> inclusion and Figure 9(ii)

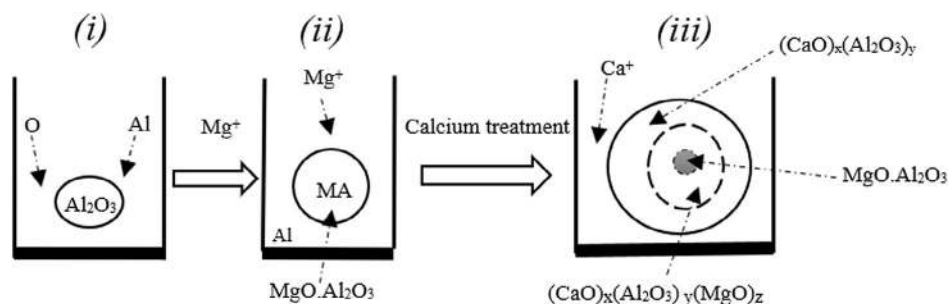


**Figure 9.** A simplified schematic evolution for oxide inclusions for Al-killed treated calcium in  $\text{CaO}\text{--}\text{Al}_2\text{O}_3\text{--}\text{MgO}$  system.<sup>[15,17,48–52]</sup>

shows the formation of solid  $\text{MgO}\cdot\text{Al}_2\text{O}_3$  spinel potential supply of excess Mg from slag or refractory in molten steel. Figure 9(iii) briefly shows a situation where during or after calcium treatment is conducted, there is the possibility of generating the multiphase calcium aluminate  $(\text{CaO})_x(\text{Al}_2\text{O}_3)_y$  system with liquid phases such as C12A7, and also potentially forming  $(\text{CaO})_x(\text{Al}_2\text{O}_3)_y(\text{MgO})_z$ , depending on the calcium treatment process and level of Mg in the melt for Al-killed steel in the molten steel.<sup>[15,17,48–52]</sup> In steelmaking, in addition to the low-melting C12A7, the relevant calcium aluminate phases are C3A and CA, because they may be present in partially liquid inclusions. Accordingly, the phase fractions of calcium aluminates and spinel in singular inclusions may vary markedly.

Most recent studies have demonstrated that using Raman spectroscopy characterizes the synthetic binary phase inclusions of calcium aluminate<sup>[39]</sup> and the binary phase containing calcium aluminate and spinel.<sup>[40]</sup> This study shows the application of Raman spectroscopy to identify and quantify the synthesized multiphase composition of  $\text{MgO}\cdot\text{Al}_2\text{O}_3\text{--}(\text{CaO})_x(\text{Al}_2\text{O}_3)_y$ , with a MAE ranging between 2.31 and 3.75 wt%. This study therefore provides a potential practical opportunity to use Raman spectroscopy to identify the oxide inclusion types and estimate their composition in a multiphase system that consists of calcium aluminate and spinel phases. Furthermore, the steel matrix is considered not to be Raman-active material. This and previous studies,<sup>[39,40]</sup> therefore, provide a reference database, which may be applied to the future measuring of steel samples using Raman spectroscopy. However, because industrial steel samples may contain some sulfide phases, such as CaS in Al-killed steel treated with calcium, future works should consider using Raman spectroscopy to characterize both laboratory and industrial steel samples containing sulfides as well.

## 4. Conclusions

This work demonstrates the applicability of Raman spectroscopy as a potential analytical technique to characterize the phase fractions for a multiphase mixture of spinel and calcium aluminate phases. The study's main findings are summarized as follows: 1) For samples that contained spinel and calcium aluminates, Raman shift region ranges identified for MA were within  $410\text{--}420\text{ cm}^{-1}$ , CA within  $545\text{--}549\text{ cm}^{-1}$  or  $526\text{--}536\text{ cm}^{-1}$ , C3A around  $756\text{--}765\text{ cm}^{-1}$ , C12A7 within  $517\text{--}522\text{ cm}^{-1}$  or  $776\text{--}781\text{ cm}^{-1}$  and were found to be the most suitable for

qualitatively estimating the specific phase present in multiphase mixtures of CA–MA–C12A7 and C3A–MA–C12A7. 2) The PLS regression-based calibration model of which features were selected with the SPA gave reasonable prediction results. The MAE of the calibration models varied between 2.31 and 3.75 wt% for the external validation dataset, depending on the phase of interest. 3) There is the prospect for practical application of time-gated Raman spectroscopy for the identification and estimation of multiphase mixtures of  $\text{MgO}\cdot\text{Al}_2\text{O}_3$  spinel calcium aluminates of C12A7, C3A, and CA in steel cleanliness studies.

## Acknowledgements

The authors acknowledge the support of I4Future doctoral programme funded by European Union's H2020 under the Marie Skłodowska-Curie grant agreement no. 713606 and Academy of Finland Proflation project (Academy of Finland, no. 311934).

## Conflict of Interest

The authors declare no conflict of interest.

## Keywords

calcium aluminates, characterizations,  $\text{MgO}\cdot\text{Al}_2\text{O}_3$  spinels, nonmetallic inclusions, Raman spectroscopy

Received: February 18, 2020

Revised: April 3, 2020

Published online: April 29, 2020

- [1] H. Tervo, A. Kajjalainen, T. Pikkarainen, S. Mehtonen, D. Porter, *Mater. Sci. Eng. A* **2017**, 697, 184.
- [2] J. Lei, H. Zhu, D. Zhao, Z. Xue, *Metals* **2019**, 9, 830.
- [3] A. L. V. Da Costa, *J. Mater. Res. Technol.* **2019**, 8, 2408.
- [4] I. Milošević, C. Garb, G. Winter, F. Grün, M. Kober, *Procedia Struct. Integr.* **2017**, 7, 327.
- [5] Z. Y. Xu, J. H. Liu, Z. J. He, Q. H. Pang, *Metalurgija* **2018**, 57, 79.
- [6] P. Yan, B. A. Webler, P. C. Pistorius, R. J. Fruehan, *Metall. Mater. Trans. B* **2015**, 46, 2414.
- [7] K. Miao, A. Haas, M. Sharma, W. Mu, N. Dogan, *Metall. Mater. Trans. B* **2018**, 49, 1612.
- [8] J. S. Park, J. H. Park, *Metall. Mater. Trans. B* **2016**, 47, 3225.
- [9] M. Jiang, X. H. Wang, W. J. Wang, *Steel Res. Int.* **2010**, 81, 759.

- [10] S. Abdelaziz, G. Megahed, I. El-Mahallawi, H. Ahmed, *Ironmak. Steelmak* **2009**, 36, 432.
- [11] J. C. S. Pires, A. Garcia, *REM, Rev. Esc. Minas* **2004**, 57, 183.
- [12] S. F. Yang, J. S. Li, Z. F. Wang, J. Li, L. Lin, *Int. J. Miner. Metall. Mater.* **2011**, 18, 18.
- [13] Y. Tabatabaei, K. S. Coley, G. A. Irons, S. Sun, *Metall. Mater. Trans. B* **2018**, 49, 2744.
- [14] N. Verma, P. C. Pistorius, R. J. Fruehan, M. S. Potter, H. G. Oltmann, E. B. Pretorius, *Metall. Mater. Trans. B* **2012**, 43, 830.
- [15] Z. Deng, M. Zhu, *ISIJ Int.* **2013**, 53, 450.
- [16] S. Yang, Q. Wang, L. Zhang, J. Li, K. Peaslee, *Metall. Mater. Trans. B*, **2012**, 43, 731.
- [17] M. Jiang, X. H. Wang, W. J. Wang, *Steel Res. Int.* **2010**, 81, 759.
- [18] P. Kaushik, H. Piolet, H. Yin, *Iron Steel Technol.* **2009**, 36, 561.
- [19] P. Kaushik, H. Piolet, H. Yin, *Iron Steel Technol.* **2009**, 36, 572.
- [20] S. Imashuku, K. Wagatsuma, *Metall. Mater. Trans. B*, **2018**, 49, 2868.
- [21] S. Imashuku, K. Ono, R. Shishido, S. Suzuki, K. Wagatsuma, *Mater. Charact.* **2017**, 131, 210.
- [22] L. Zhang, B. G. Thomas, *ISIJ Int.* **2003**, 43, 271.
- [23] S. Li, L. H. Hihara, *J. Raman Spectrosc.* **2017**, 48, 137.
- [24] C. Hirlimann, M. Jouanne, C. Forriès, *J. Raman Spectrosc.* **1992**, 23, 315.
- [25] H. G. M. Edwards, *Modern Raman Spectroscopy—A Practical Approach*, John Wiley and Sons, Chichester **2005**, p. 210.
- [26] J. R. Ferraro, K. Nakamoto, C. W. Brown, *Introductory Raman Spectroscopy*, 2nd ed, Elsevier, Cambridge **2003**, p. 15.
- [27] A. Dandeu, B. Humbert, C. Carteret, H. Muhr, E. Plasari, J. M. Bossoutrot, *Chem. Eng. Technol.* **2006**, 29, 221.
- [28] J. H. Giles, D. A. Gilmore, M. B. Denton, *J. Raman Spectrosc.* **1999**, 771, 767.
- [29] C. A. F. de Oliveira Penido, M. T. T. Pacheco, E. H. Novotny, I. K. Lednev, L. Silveira, *J. Raman Spectrosc.* **2017**, 48, 1732.
- [30] N. Chieng, S. Rehder, D. Saville, T. Rades, J. Aaltonen, *J. Pharm. Biomed. Anal.* **2009**, 49, 18.
- [31] S. Dash, R. K. Sahoo, A. Das, S. Bajpai, D. Debasish, S. K. Singh, *J. Alloys Compd.* **2017**, 726, 1186.
- [32] A. Chopelas, A. M. Hofmeister, *Phys. Chem. Miner.* **1991**, 18, 279.
- [33] L. Black, C. Breen, J. Yarwood, C. S. Deng, J. Phipps, G. Maitland, *J. Mater. Chem.* **2006**, 16, 1263.
- [34] M. Ruzsak, S. Witkowski, P. Pietrzyk, A. Kotarba, Z. Sojka, *Funct. Mater. Lett.* **2011**, 4, 183.
- [35] D. R. Neuville, G. S. Henderson, L. Cormier, D. Massiot, *Am. Mineral.* **2010**, 95, 1580.
- [36] D. Torrén-Martín, L. Fernández-Carrasco, S. Martínez-Ramírez, J. Ibáñez, L. Artús, T. Matschei, *J. Am. Ceram. Soc.* **2013**, 96, 3589.
- [37] F. Gyakwaa, M. Aula, T. Alatarvas, T. Vuolio, M. Huttula, T. Fabritius, *ISIJ Int.* **2019**, 59, 1846.
- [38] F. Gyakwaa, M. Aula, T. Alatarvas, T. Vuolio, Q. Shu, M. Huttula, *ISIJ Int.* **2020**, <https://doi.org/10.2355/isijinternational.ISIJINT-2019-576>.
- [39] J. H. Park, *Metall. Mater. Trans. B* **2013**, 44B, 938.
- [40] T. Lipiäinen, J. Pessi, P. Movahedi, J. Koivistoinen, L. Kurki, M. Tenhunen, J. Yliruusi, A. M. Juppo, J. Heikkonen, T. Pahikkala, C. J. Strachan, *Anal. Chem.* **2018**, 90, 4832.
- [41] J. R. Beattie, J. V. Glenn, M. E. Boulton, A. W. Stitt, J. J. McGarvey, *J. Raman Spectrosc.* **2009**, 40, 429.
- [42] I. Guyon, A. Elisseef, *J. Mach. Learn. Res.* **2003**, 3, 1157.
- [43] X. B. Zou, J. W. Zhao, M. J. W. Povey, M. Holmes, H. P. Mao, *Anal. Chim. Acta* **2010**, 667, 14.
- [44] K. Baumann, *Trends Anal. Chem.* **2003**, 22, 406.
- [45] M. C. U. Araújo, T. C. B. Saldanha, R. K. H. Galvão, T. Yoneyama, H. C. Chame, V. Visani, *Chemom. Intell. Lab. Syst.* **2001**, 57, 65.
- [46] P. Geladi, R. Kowalski, *Anal. Chim. Acta* **1986**, 185, 1.
- [47] P. McMillan, B. Piriou, *J. Non-Cryst. Solids* **1983**, 55, 221.
- [48] C. Liu, D. Kumar, B. A. Webler, P. C. Pistorius, *Metall. Mater. Trans. B* **2020**, 51, 529.
- [49] H. Mu, T. Zhang, R. J. Fruehan, B. A. Webler, *Metall. Mater. Trans. B* **2018**, 49, 1665.
- [50] J. H. Shin, J. H. Park, *Metall. Mater. Trans. B* **2017**, 48, 2820.
- [51] J. H. Shin, Y. Chung, J. H. Park, *Metall. Mater. Trans. B* **2016**, 48, 46.
- [52] T. Zhang, Y. Min, C. Liu, M. Jiang, *ISIJ Int.* **2015**, 55, 1541.